Lab on a Chip

ROYAL SOCIETY OF CHEMISTRY

PAPER

View Article Online
View Journal | View Issue

Check for updates

Cite this: *Lab Chip*, 2020, **20**, 414

A self-driven microfluidic surface-enhanced Raman scattering device for Hg^{2+} detection fabricated by femtosecond laser†

Xiuyun Li,[ab] Gan Yuan,[ab] Weili Yu,[a] Jun Xing,[ab] Yuting Zou,[ab] Chen Zhao,[ab] Wenchi Kong,[ab] Zhi Yu*[a] and Chunlei Guo *[ac]

Received 5th September 2019,
Accepted 5th December 2019

DOI: 10.1039/c9lc00883g

rsc.li/loc

In this paper, we proposed a novel approach for rapid and flexible fabrication of self-driven microfluidic surface enhanced Raman scattering (SERS) chips for quantitative analysis of Hg^{2+} by femtosecond laser direct writing. In contrast to traditional microfluidic chips, the microchannels of the device can drive a liquid sample flow without external driving force. The sample flow speed is tunable since the wettability and capillarity properties of the channels, which depend on the roughness and the inner diameter of the microchannels, can be controlled by optimizing the laser processing parameters. The SERS active detection sites, which exhibit high enhancement effects and fine reproducibility, were integrated through the femtosecond laser-induced periodic surface structures (LIPSS), followed by 30 nm Ag deposition. The SERS performance of the as-prepared microfluidic SERS detection chip was studied with R6G as probe molecules. The quantitative analysis of Hg^{2+} was realized by simply injecting the Hg^{2+} sample and the probe molecules R6G from the two inlets, separately, and collecting the SERS signal at the detection site. The lowest detection limit for Hg^{2+} is 10^{-9} M. It should be mentioned that this study is not only limited to Hg^{2+} quantitative analysis, but is also mainly aimed to develop a new technique for the design and fabrication of novel self-driven microfluidic devices depending on practical application requirements.

Introduction

Over the past two decades, microfluidic chips, also known as lab-on-a-chip (LOC) systems, have drawn significant research interest due to their numerous advantages compared to macroscopic apparatuses including low cost, high sensitivity, short reaction times, portability and multi-function integration.[1–5] As a result, microfluidic platforms have been increasingly applied to chemical analytics,[6] chemical synthesis,[7] biological cellular assays,[8,9] biotransformation,[10] optical detection[11] and so on. Microfluidic chips are capable of disposing and manipulating fluids at the micron level, but the small area also prohibited the use of such chips with some conventional detection apparatuses (such as PL, UV fluorescence) which are only applicable for targets with a much bigger size.

This problem can be solved by introducing surface enhanced Raman scattering (SERS) techniques into microfluidic analysis. SERS is an excellent detection technique that is appropriate for microfluidic chips and SERS based detection can be realized in a limited space with trace amounts of the samples, due to its low reagent consumption and ultrahigh spectroscopic sensitivity.[12,13] In addition, SERS detection exhibits some other outstanding advantages, such as extremely narrow peak widths, multivariate analysis, good stability and high selectivity.[14,15] Moreover, SERS signals can reveal the fingerprint of molecules by showing the rotational, vibrational and other internal motion information of molecules on substrates.[16,17]

The combination of microfluidics and SERS not only enriches the variety of microfluidic chips but also extends the application of SERS. Microfluidic SERS devices have broadened the prospects of application in environmental analysis, biomolecule detection, *etc.*[18,19] Among these applications of microfluidic SERS devices, the detection of metal ions is a very important part, such as Hg^{2+}, Pb^{2+}, *etc.*[20] The analysis of Hg^{2+} is quite important due to its high toxicity. Thus, the detection of Hg^{2+} based on SERS microfluidic chips or SERS substrates fabricated with microfluidic devices has also been extensively developed.[20–24] Chung *et al.* has reported using aptamer-modified Au/Ag core–shell nanoparticles to detect Hg^{2+} on a SERS-based microfluidic device.[23]

---

[a] *The Guo China-US Photonics Laboratory, State Key Laboratory for Applied Optics, Changchun Institute of Optics, Fine Mechanics and Physics, Chinese Academy of Sciences, Changchun, 130033, China. E-mail: zhiyu@ciomp.ac.cn*
[b] *University of Chinese Academy of Sciences, Beijing 100049, China*
[c] *The Institute of Optics, University of Rochester, Rochester, NY 14627, USA. E-mail: guo@optics.rochester.edu*

† Electronic supplementary information (ESI) available. See DOI: 10.1039/c9lc00883g

A shortcoming of using colloid nanoparticles as the SERS detection substrate is the unwanted mixing between the nanoparticles and samples in the channel. The random aggregation of the nanoparticles will affect the sensitivity and reproducibility.[25] To avoid this defect, attempts have been made to avoid this effect by directly integrating SERS active substrates into the channel. For instance, Yan *et al.* proposed a two-step photo-reduction method to integrate silver nanoparticles as an *in situ* SERS active substrate. The Ag nanoparticles substrate in their study realized on-chip single molecule spectroscopy with high repeatability.[26] Bai *et al.* embedded a Ag–Cu alloy in a 3D microfluidic channel by a femtosecond laser. Their research exhibited real-time detection of toxic substances with good reproducibility.[27] However, the integration of SERS substrates is relatively complex.

Furthermore, fluids flowing in microchannels usually rely on an external driving force from a syringe pump. To simplify microfluidic devices, self-driven microfluidic fabrication techniques have progressed continuously and an increasing number of scientific researchers have developed new microfluidic technologies driven by the capillary effect (Table S1†). The materials used in traditional microfluidic devices, such as glass, polydimethylsiloxane and other polymers,[28–30] are not suitable for fabricating self-driven chips. For example, there are some reports about PDMS self-driven microfluidic sensors. But, the fabrication of these devices is relatively complicated and the self-driven properties must be realized by further hydrophilic modification. Cheng *et al.* demonstrated a self-driven PDMS microfluidic chip to perform automated qualification of live bacillus Calmette–Guerin (BGG) by fluorescence detection and the self-driven properties were realized by design special capillary structures with additional baking.[31] As for paper or paper-like material based self-driven microfluidic devices, colorimetry is always utilized as an analysis tool for detection, which exhibit relatively low sensitivity and are always not recyclable.[32] Based on the current situation, we put forward a one-step method to fabricate self-driven microchannels by femtosecond laser direct writing (FLDW).

Femtosecond lasers have been used for the fabrication of microfluidic chips.[33–35] The polymer-based microfluidic devices can be fabricated by femtosecond lasers due to nonlinear adsorption.[36,37] It possesses many advantages for materials processing such as low heat diffusion, high-precision processing capacity and high reproducibility.[38,39] All these advantages make femtosecond lasers a powerful tool for high precision micro–nano machining techniques.[40] Thus, femtosecond lasers have already been widely used for the fabrication of functional materials with micro–nano structures, such as superhydrophobic and superhydrophilic surfaces, black metal materials, colored metals, *etc.*[41–44] In previous reports, our group has fabricated superhydrophilic silicon or platinum surfaces by femtosecond laser, which provide Si or Pt superwicking properties. As a result, fluids can overcome gravity and flow upward on a vertically positioned processed surface.[45–47] The study on the surface wettability by femtosecond laser provides a new way to control the flow of liquid samples and the materials used for the fabrication are not limited to transparent materials or polymer materials, which shows many more advantages for the fabrication of new type microfluidic devices.[48] Another attractive phenomenon is laser-induced periodic surface structures (LIPSS), which are able to fabricate micro–nano structures on materials' surfaces by FLDW.[49] LIPSS can form 1D or 2D micro–nano structures on insulators, polymers, semiconductors and metals depending on different material properties, processing parameters and experimental environments.[50,51] The micro–nano structures show many attractive characteristics such as special optical properties,[52] SERS[53] and surface wettability.[54]

In this paper, a simple and convenient method is proposed to integrate a new type of self-driven microfluidic SERS detection chip onto Si by FLDW. The construction of the predesigned structure of the microfluidic devices was performed on a Si slide. The key points for the fabrication are as follows: 1. selecting suitable laser fabrication parameters and ensuring spontaneous liquid sample flow through the microchannel with tunable flowing velocities; 2. optimizing the surface micro–nano structure to provide excellent SERS performance with high reproducibility and stability. Based on the above criteria, we first prepared the self-driven microchannels by controlling the laser parameters and built up the relationship between the liquid flow properties and the processing conditions. Then, periodic nano ripple structures were generated at the predesigned SERS detection position, and the influence of laser parameters on the SERS properties was studied to achieve an optimal detection effect. Finally, the quantitative analysis of Hg^{2+} was performed using the self-driven microfluidic SERS detection platform.

Experimental section

Materials

Rhodamine 6G (R6G, $C_{28}H_{31}N_2O_3Cl$), mercuric nitrate ($Hg(NO_3)_2$) copper(II) acetate ($Cu(CH_3COO)_2$), sodium acetate (CH_3COONa), zinc acetate dihydrate ($Zn(CH_3COO)_2·2H_2O$), magnesium acetate tetrahydrate ($Mg(CH_3COO)_2·4H_2O$), lead(II) acetate trihydrate ($Pb(CH_3COO)_2·3H_2O$), potassium acetate (CH_3COOK) and *n*-hexane ($CH_3(CH_2)_4CH_3$) were purchased from Sigma-Aldrich. Anhydrous ethanol (CH_3CH_2OH) was purchased from Beijing Chemical Works. Crystalline silicon (Si) slices (100) were purchased from Sibranch Electronic Science and Technology Company and *n*-octadecyltrichlorosilane ($C_{18}H_{37}C_{l3}Si$) was purchased from Aladdin. Deionized water (18.0 MΩ cm^{-1}) was used during the experiment.

Fabrication of microchannels on Si by femtosecond laser direct writing

Firstly, a Si wafer was put in a UV Ozone Cleaning System for 15 min (Fig. 1A). The Si wafer was then immersed in *n*-octadecyltrichlorosilane (40 μL) dissolved in *n*-hexane (20

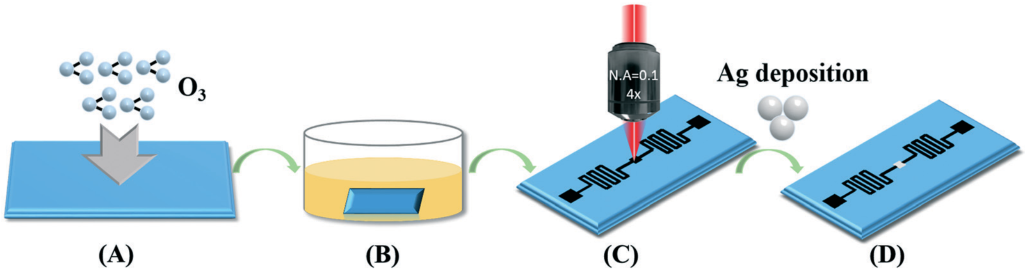

Fig. 1 Schematic for the fabrication of the Si microfluidic SERS chips.

mL) (Fig. 1B). After half an hour, it was washed with anhydrous ethanol and dried with a N_2 flow. The contact angle of the Si wafer changed from 34° (Fig. S1A†) to 104° (Fig. S1B†) after the hydrophobic treatment.

A laser beam was irradiated onto the Si surface vertically with an appropriate power, defocused position and scanning speed, as shown in Fig. S2.† Microfluidic channels and two square (2×2 mm^2) inlets were obtained as shown in Fig. 1C.

Integration of a SERS active detection site onto the Si microfluidic chip

Firstly, a 1×1 mm^2 square area with micro–nano structures was fabricated by femtosecond laser at the joint of the microchannels (Fig. 1C). After immersing in an ultrasonic bath with deionized water for 15 min, a 30 nm Ag film was deposited on the as-prepared square area to form Ag micro–nano structures, which would be used as the SERS active detection site (Fig. 1D). The SERS activity of the substrate was controlled by altering the surface morphology of the micro–nano structures with different laser processing parameters.

SERS measurements based on the Si microfluidic chip

The SERS activity was tested by adding R6G solutions with concentrations ranging from 10^{-3} to 10^{-9} M. The quantitative analysis of Hg^{2+} was further proposed by adding a 10^{-3} M R6G solution as a probe from one inlet and Hg^{2+} solutions with different concentrations from another inlet. SERS spectra of R6G molecules were collected at the SERS active site.

Sample characterization

The light source for laser fabrication was a femtosecond Ti: sapphire chirped-pulse amplifier system (Spitfire Ace, Spectra Physics) as a photosource was employed for laser fabrication. It delivers a pulse duration of 35 fs with a central wavelength of 800 nm and a repetition rate of 1 kHz. The maximum

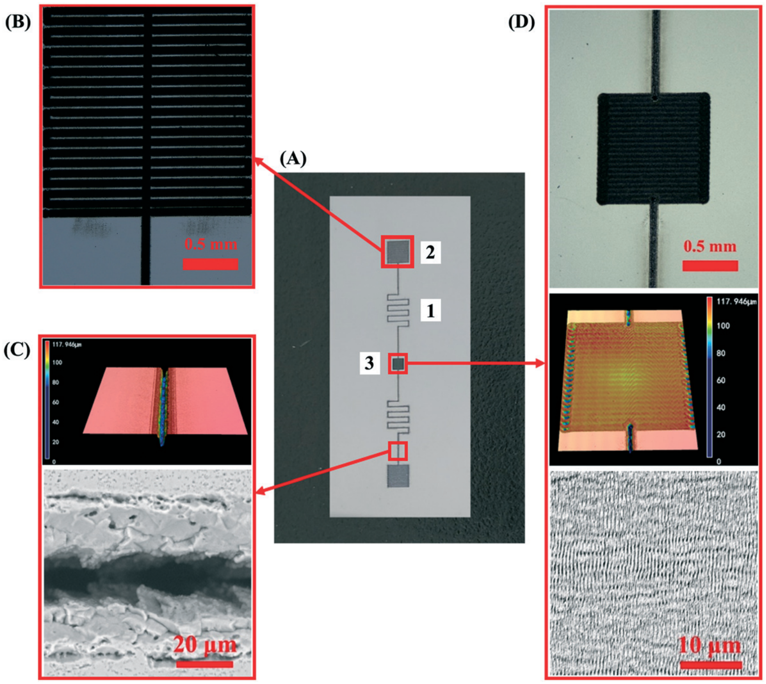

Fig. 2 (A) Photograph of the whole microfluidic platform. (B) Optical image of the 2×2 mm^2 square inlet. (C) 3D and SEM images of the microchannel. (D) Optical, 3D and SEM images of the SERS active site.

average power is 5 W and the laser beam was focused by a 4× objective lens with a numerical aperture (NA) of 0.1. The diameter of the laser beam is around 6.62 μm after being focused by the 4× objective lens.

3D microchannels and square graphs were measured using a KEYENCE VK-X200 3D laser scanning microscope. Scanning electron microscopy (SEM) analysis was carried out using a Phenom ProX purchased from PHENOM WORLD. Raman spectra were gathered using a LabRAM HR Evolution Raman spectrometer (Horiba Jobin Yvon), with an excitation wavelength of 532 nm and integration time of 1 s. The contact angle was measured using a POWEREACH JC2000D3.

Results and discussion

Surface morphology characterization of the self-driven microfluidic devices

The self-driven microfluidic SERS devices were successfully processed by femtosecond laser direct writing. Fig. 2A shows the full image of a self-driven microfluidic chip manufactured with a femtosecond laser in air. The device consists of three parts: 1. microfluidic channels; 2. inlet; 3. SERS active detection site.

Fig. 2B shows the optical photograph of a 2 × 2 mm^2 square which served as an inlet for the chip. During the processing, 2 mm transverse scanning was repeated after a longitudinal motion of the sample of 2 mm with a step length of 100 μm. Fig. 2C shows the 3D optical graph and SEM image of a part of the microfluidic channel fabricated by FLDW with a total length of 21 mm. Fig. 2D shows the surface morphology of the SERS active detection site of the microfluidic chip. It can be seen that the SERS active site was integrated at the joint of the micro-channel, which ensures the mixture of the liquid samples from the two inlets at the detection site. The SEM image indicates that the nano ripples were formed at the surface to ensure strong SERS enhancement and high reproducibility.

Self-driven property study of the microfluidic channels

The fluid driven capability of the microfluidic channels was studied by measuring the flow velocities of water along the microchannels. As the video shows, water can flow spontaneously along the microchannel. The self-driven movement of water in the Si microfluidic channel is attributed to the capillary action. The driving force of the attraction between the fluid and solid capillary surface mainly comes from surface tension and the wettability properties between the liquid and the capillary surface. The wicking dynamics on capillary tubes are briefly described. In general, surface tension plays a key role in the spontaneous movement of liquid samples. If the capillary tube is inserted into infiltrative fluid, the liquid level of the tube will rise. In contrast, if it is inserted into non-infiltrative fluid, the liquid level of the tube will decline. Thus, for Si, water is an infiltrative liquid and so the surface tension enables it to flow along the microchannel. It is also known that the surface roughness plays a significant role in the surface wettability. According to Wenzel's model, increasing the surface roughness will increase the hydrophilicity or hydrophobicity.[55] The microfluidic channel on Si exhibits capillary properties, which were affected by the depth-to-width ratio of the channel. Meanwhile, the micro–nano structures on the microchannel surface enhanced the roughness of the microchannel and the hydrophilicity of the microchannel was improved (Fig. S1C†). As a result, the microchannel can drive the liquid sample flow spontaneously. Therefore, the self-driven motion in the microfluidic channel can be attributed to the following factors: (1) the microfluidic channel fabricated by a femtosecond laser exhibits a capillary effect. (2) The enhanced roughness of the Si (which is infiltrated with water) surface by laser processing strengthened the driving force for self-driven flow. (3) Due to the hydrophobic treatment on the Si surface, the microfluidic channel is hydrophilic and so, the water is confined in the channel.

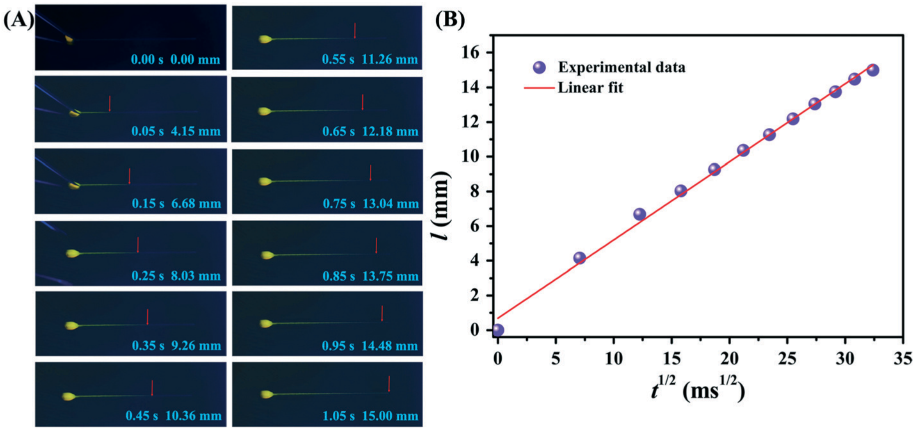

Fig. 3 The images of the R6G aqueous solution flowing in the microchannel with different times under UV light (A) and the plot of the flowing distance (l) *versus* $t^{1/2}$ (B).

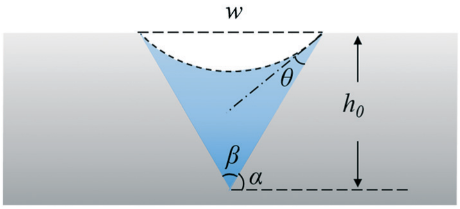

Fig. 4 The schematic of a V-groove.

To better study the wicking dynamics in our experiment, the liquid samples' flowing states along the microchannel were recorded. As shown in Fig. 3A, an aqueous solution of R6G was injected into the microchannel and the images with the flowing distances at different times were recorded under UV light for a better view. The distance l was plotted *versus* $t^{1/2}$ and the result is shown in Fig. 3B. We can conclude from the figure that the spreading distance linearly depends on $t^{1/2}$ for our microchannel.

In our work, the shape of the microchannel fabricated with a femtosecond laser is a V-groove (Fig. S4†). As reported, Rye *et al.* proposed a wicking dynamics model in a V-groove channel (Fig. 4), which shows a similar form with the Washburn equation.[56] The model was created based on the theory of an interfacial energy balance. Meanwhile, it takes the balance of the surface tension driving force and the Poiseuille flow viscous dissipation force and makes a series of assumptions in a V-groove channel. As a result, Rye arrived at a model of the V-groove as:

$$l^2 = K(\alpha,\theta)\frac{\gamma h_0}{\mu}t = \frac{\cos(\theta)-\cos(\alpha)}{2\pi\sin(\alpha)}\frac{\gamma h_0}{\mu}t \qquad (1)$$

where α is the modeling variable angle related to the groove apex angle β ($\beta = \pi/2 - \alpha$) and h_0 is the depth of the V-channel. According to the equation, the liquid flowing distance (l) in the channel is in direct proportion to $t^{1/2}$. In our case, the experiment shown in Fig. 3B well matched with the Rye model (eqn (1)).

These results lead to a belief that in our system, the liquid flowing in the microchannels processed by femtosecond laser is indeed from the capillarity. In addition, the model reveals a significant dependence of liquid spreading rate on the geometry and the wettability of the V-groove channel. When the laser processing parameters are altered, the roughness of the surface and the geometry of the microchannel will be changed. With the height (h_0), width and roughness altering, α and θ will be changed. Thus, according to eqn (1), the liquid wicking velocity in the microchannel will be affected. As a result, the liquid flowing velocity in the microchannel fabricated with a femtosecond laser can be controlled *via* tuning the parameters of the femtosecond laser.

We further studied the shape and the micro–nano structure of the microchannel using different laser processing parameters. Table S1† shows the statistical results for the flow velocities and depth-to-width ratios of the channels fabricated by laser direct writing under different processing conditions, which were calculated from the measured results using a laser scanning microscope. The morphology of the microchannels was characterized using a 3D laser scanning microscope and a SEM. It was observed that the microfluidic channel has a symmetrical shape with the deepest depth in the middle position due to Gaussian light pulses. The results are exhibited in Fig. S5† where A–C were fabricated with different laser fluences, 4.76 J cm^{-2}, 7.14 J cm^{-2}, and 9.52 J cm^{-2}, and a–e were obtained with various scanning velocities, ranging from 0.1 to 0.9 mm s^{-1}. From Fig. S5,† we conclude that, under the same scanning velocity, the depth of the microchannel increases with the laser pulse energy. This is expected since the ablation capacity increases with laser fluence. At the same pulse energy, the depth of the microfluidic channel increases when the scanning velocity decreases. This is because the target material will be ablated more severely with a longer contact time.

The relationship between the water flowing speed and the laser processing parameters (laser fluence and scanning velocity) are plotted in Fig. 5A. The results indicate that the flow speed increases as the laser fluence increases and the flow speed decreases as the laser scanning velocity increases. In other words, these observations are consistent with those mentioned in the previous paragraph.

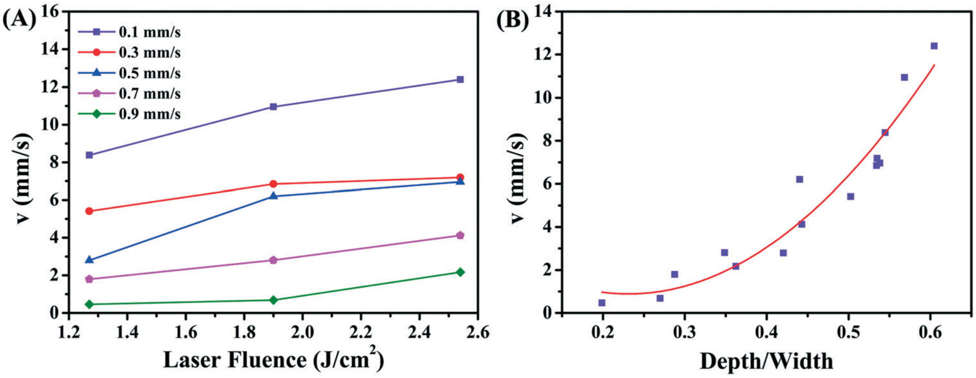

Fig. 5 The relationship between liquid flow velocity and laser fluence (A) and liquid flow velocity and depth-to-width ratio (B) on the microfluidic channels obtained using different processing parameters.

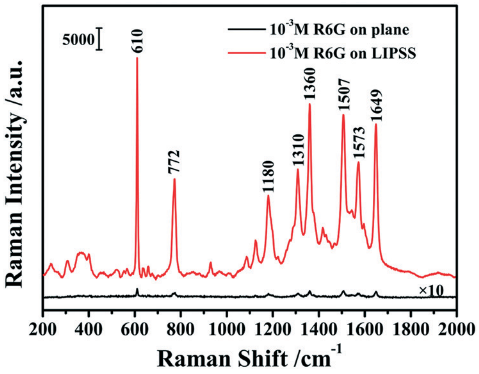

Fig. 6 Raman spectra of R6G (concentration 10^{-3} M) on the LIPSS structure and planar Si.

The relationship between the depth-to-width ratio and fluid velocity is plotted in Fig. 5B. It is found that the fluid velocity increases with increasing depth-to-width ratio within a certain range. According to the results, a laser fluence of 9.52 J cm^{-2} and scanning speed of 0.1 mm s^{-1} were utilized to fabricate the microchannels on the final chip used for the following applications.

Furthermore, the repeatability and stability of the microchannel were studied. Fig. S6A† shows the result of the flow velocity with 34 times of repeated measurements for the same channel. The flowing velocity only decreases by 14% after 34 times of measurements which indicates the good repeatability of the microfluidic channel. Fig. S6B† shows a 21-day continuous measurement for three different channels. After 21 days, the flow rates decreased to 98.75%, 90.99% and 96.00%, respectively. The result indicated that microfluidic channels fabricated with a femtosecond laser exhibits pretty good stability.

SERS study of the femtosecond laser-induced periodic surface structures

As mentioned above, a femtosecond laser was used to integrate a SERS active detection site at the joint of the microchannel. It possesses mainly two advantages for SERS active detection site integration. First, the femtosecond laser shows high processing accuracy, which ensures the integration of the SERS active detection site at the expected position of the microfluidic devices more accurately and flexibly. Second, the femtosecond laser can induce the formation of micro–nano structures at the surface of the materials, which can provide a strong electromagnetic field for SERS detection. In particular, LIPSS can significantly improve the reproducibility and stability of the SERS measurements. In this study, nano ripple structures were fabricated at the SERS active site after optimizing the laser processing parameters. The orientation of the nano ripples is perpendicular to the polarization of the incident beam and the periodicity is around 600 nm, which is more than 50% of the laser wavelength of 800 nm (75%). Hence, the periodic nanograting fabricated on the Si surface is classified as low-spatial-frequency LIPSS.[57]

The SERS activity of the prepared substrate was studied with the SERS spectra of R6G attached to a Si slice without laser processing as a comparison. As shown in Fig. 6, the SERS intensity of R6G molecules adsorbed on the LIPSS SERS substrate is much stronger than that on a flat surface due to the strong electromagnetic field of the nano ripples. The assignment of the Raman bands is shown in Table S3.†[58]

The laser parameters used in the fabrication will affect the formation of the micro–nano structures and further affect the SERS activity. Thus, the SERS properties of the substrate with different laser fabrication parameters were studied. Fig. S7† shows the SEM characterization results of the nanostructure with different laser processing parameters and the corresponding SERS spectra of R6G molecules. The statistical results of the SERS spectra are shown in Fig. 7. The error bars indicate the standard deviation of the SERS intensity with 5 repeated measurements. The results indicate that the laser scanning velocity strongly affects the micro–nano structure and thus the SERS effect. During fabrication with a low laser scanning velocity (0.1 mm s^{-1}, Fig. S7A a–e†), the substrate was ablated severely due to the long contact time between the laser beam and the Si slice. Thus, the surface exhibits irregular structures, which results in much worse reproducibility and stability for the SERS signal. When increasing the scanning velocity, the LIPSS appears and lead to a great field enhancement factor for SERS. Unsurprisingly, this also

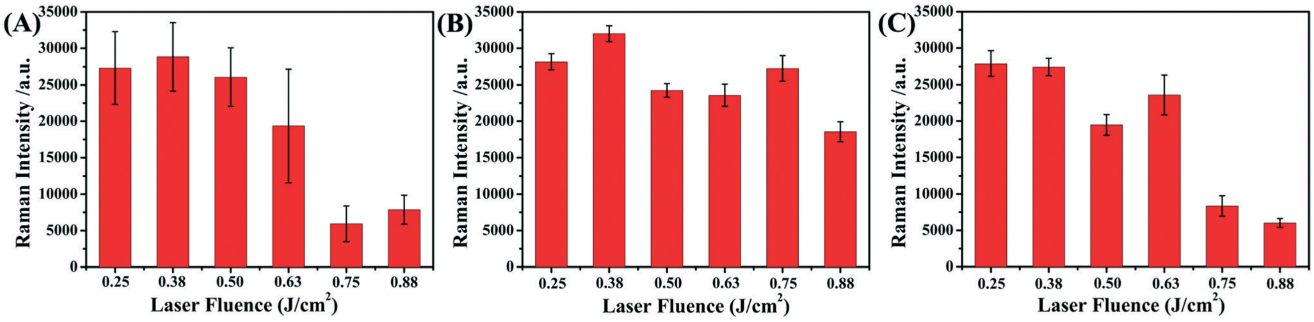

Fig. 7 SERS intensities of the band at 1360 cm^{-1} of R6G molecules adsorbed on the substrates fabricated with laser fluence ranging from 0.25 to 0.88 J cm^{-2} and different laser scanning velocities: (A) 0.1 mm s^{-1}, (B) 0.5 mm s^{-1}, and (C) 1 mm s^{-1}.

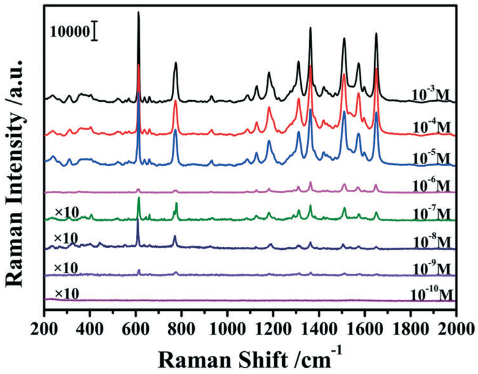

Fig. 8 SERS spectra of R6G molecules with concentrations ranging from 10^{-3} to 10^{-10} M.

improves the reproducibility and stability for the SERS signal due to the uniformity and reproducibility of the pattern itself.

The better reproducibility is attributed to the more uniform distribution of the 2D periodic structures. Taking enhanced capacity and reproducibility into account, we choose the substrate (fabricated using a scanning velocity of 0.5 mm s^{-1} and laser fluence of 0.38 J cm^{-2}) for further study due to its highly enhanced capability and great reproducibility. After deposition of a 30 nm Ag film, the SERS active site was prepared. EDS analysis was conducted to analyze the elemental composition of pristine LIPSS and the substrate after Ag deposition (Fig. S8†).

In order to further study the reproducibility of the SERS substrate, seven substrates were fabricated using the same processing parameters and the SERS signal of 10^{-3} M R6G on them was collected. The intensity of the Raman band at 1360 cm^{-1} is plotted as shown in Fig. S9.† The calculated relative standard deviation (RSD) reaches 5.7%.

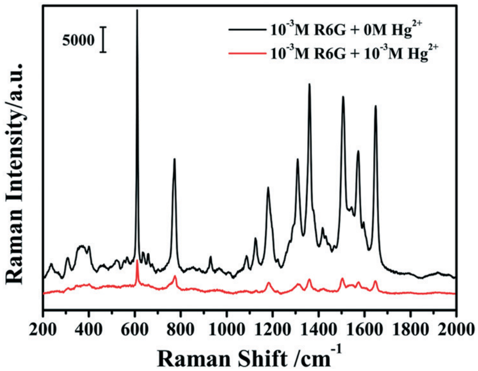

Fig. 9 SERS spectra of R6G on the substrate with and without the addition of Hg^{2+} with a concentration of 10^{-3} M.

Fig. 8 shows the SERS spectra of R6G with concentrations ranging from 10^{-3} M to 10^{-10} M. The spectral intensity from 10^{-7} M to 10^{-10} M is amplified by an order of magnitude. The signal intensity decreases with the R6G solution concentration decreasing and disappears at 10^{-10} M, while the characteristic bands assigned to R6G molecules can still be observed at a 10^{-9} M concentration.

Application of the microfluidic SERS detection platform in the detection of Hg^{2+}

Mercury is one of the most toxic heavy metals and has extensive applications in industrial production.[59] Due to various types of industrial activities, the chance of the human body being exposed to mercury has been increasing rapidly. For example, Hg^{2+} contamination in drinking water and irrigation water is a serious threat to human health. Therefore, a sensitive method for Hg^{2+} detection is needed and we demonstrate that our microfluidic SERS chip can be utilized for this purpose. A 1 μL 10^{-3} M R6G solution was added from an inlet as a probe and 1 μL Hg^{2+} solution dissolved in water was added from another inlet. After mixing these two solutions at the SERS active point, SERS spectra were collected.

Fig. 9 shows the SERS spectra of R6G molecules with the addition of 0 M and 10^{-3} M Hg^{2+}. The SERS intensity of the R6G molecules decreases significantly after adding Hg^{2+}. This is mainly due to the content change of R6G molecules adsorbed on the SERS active point. As shown in Fig. 10A, when the fluid with R6G molecules flow into the SERS active point, the Raman signal of R6G was dramatically enhanced by the Ag nano ripples. However, with the addition of Hg^{2+}, the R6G molecules were desorbed from the SERS active point due to the stronger binding force of Hg^{2+} with R6G than that with Ag (Fig. 10B). As a result, small amounts of R6G molecules were left on the Ag surface and the SERS intensity decreased. This result indicates that the prepared microfluidic chip is suitable for Hg^{2+} detection.

The quantitative analysis of Hg^{2+} was further performed with different concentrations of Hg^{2+} solutions added into the microfluidic chip. As Fig. 11 shows, with decreasing Hg^{2+} concentration, the SERS intensity of R6G molecules

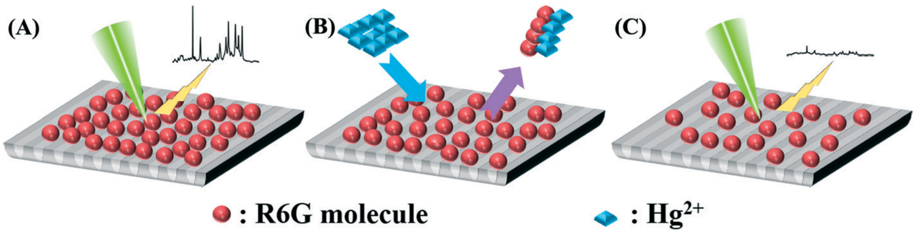

Fig. 10 The schematic of the detection of Hg^{2+}.

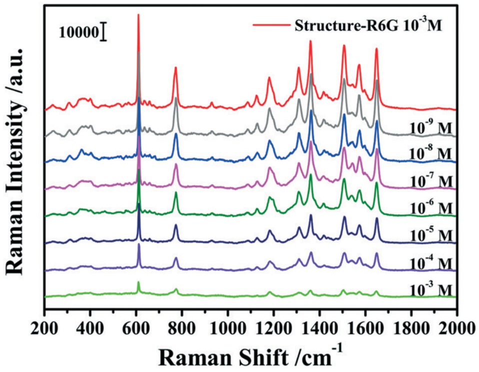

Fig. 11 SERS spectra of R6G molecules after adding Hg^{2+} with concentrations ranging from 10^{-3} to 10^{-9} M.

increased. As discussed above, with a higher concentration of Hg^{2+} solution, Hg^{2+} can combine with more R6G molecules leaving fewer R6G molecules adsorbed on the substrate resulting in lower SERS intensity. In contrast, Hg^{2+} with a low concentration can combine with fewer R6G molecules, and the intensity of the R6G spectra will increase.

The SERS intensity of the band at 1306 cm^{-1} was chosen to plot the calibration curves for the quantitative analysis of Hg^{2+}. The intensity of the band at 1306 cm^{-1} as a function of Hg^{2+} concentration on a semi-log scale is plotted over the concentration ranging from 10^{-3} M to 10^{-9} M in Fig. 12A. The error bars indicate the relative standard deviation of 5 repeated measurements. The relationship between the logarithm of Hg^{2+} concentration and the Raman intensity of the band at 1360 cm^{-1} is linear ($Y = 4379.63X - 10307.30$; $R^2 = 0.9901$), where X represents the logarithm of Hg^{2+} concentration and Y stands for the Raman intensity of R6G at 1360 cm^{-1}. Fig. 12B shows the intensity of the Raman band at 1360 cm^{-1} for 0 M and 10^{-9} M Hg^{2+} in order to affirm the limit of detection (LOD). The red line is the limit of detection in Fig. 12B, which indicates that the lowest LOD is 10^{-9} M, and the comparisons of the detection level of Hg^{2+} with those of reported articles are shown in Table S4.†

In order to evaluate the selectivity of the microfluidic chip to Hg^{2+}, an anti-interference experiment was performed with several metal ions (Cu^{2+}, Na^{+}, Zn^{2+}, Mg^{2+}, Pb^{2+}, K^{+}) as reference. As demonstrated in Fig. S10,† the SERS intensity of R6G molecules shows no obvious change with the addition of 10^{-2} M metal ions compared to that with the addition of 10^{-4} M Hg^{2+}. This indicates that the presence of other metal ions rarely influenced the detection of Hg^{2+} even when the ion concentration is two orders of magnitude higher than that of Hg^{2+}. It proves that the microfluidic chip can be used for the selective detection of Hg^{2+}. A practical application for the detection of Hg^{2+} is demonstrated as follows. Hg^{2+} samples at three different concentrations (5×10^{-4} M, 5×10^{-5} M and 10^{-5} M) were added to lake water and tap water. The SERS spectra of these samples were then measured. As shown in Table S5,† the average recoveries of these three concentrations determined by this method were 99.3%, 92.7%, and 96.4% for tap water and 89.8%, 100.7%, and 105.4% for lake water, respectively. The results indicate that the microfluidic SERS chip is also suitable for the real sample detection of Hg^{2+}.

Conclusions

In conclusion, we proposed a simple and convenient way for fabricating a self-driven microfluidic SERS detection chip by femtosecond laser direct writing. The prepared microfluidic chip exhibits the following advantages: 1. the high processing accuracy and high pulse energy of a femtosecond laser makes the microfluidic chip integration more precise and flexible; 2. the shape and wettability of the microchannel can be tuned by optimizing the processing parameters of the femtosecond laser and the liquid sample flowing spontaneously along the microchannel without an external force due to the capillarity and hydrophilic properties of the channel; 3. femtosecond laser induced periodic nano ripples can provide strong Raman enhancement with better reproducibility and stability. The prepared self-driven microfluidic chip was further used for the quantitative analysis of Hg^{2+} with R6G molecules as the probe.

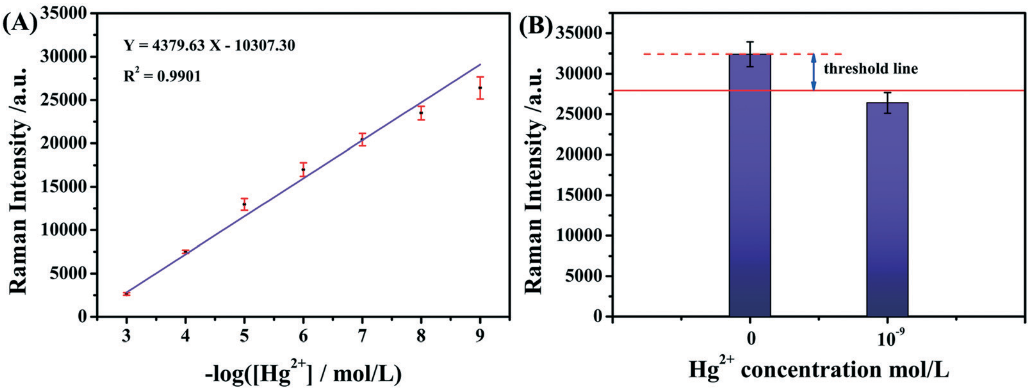

Fig. 12 (A) Quantitative analysis line plot of the SERS intensity of the band at 1306 cm^{-1} with the concentration of Hg^{2+} ranging from 10^{-3} to 10^{-9} M. (B) SERS intensity of the band at 1306 cm^{-1} with the addition of 0 and 10^{-9} M Hg^{2+}. The error bars indicate the RSD of 5 repeated measurements.

The detection limit can reach 10^{-9} M. It should be mentioned that the microfluidic chip can be used for more than Hg^{2+} analysis. The design and fabrication of new types of microfluidic devices for more practical applications can be realized depending on the requirements of practical applications.

Conflicts of interest

There are no conflicts to declare.

Acknowledgements

This research was supported by the National Key R&D Program of China (2017YFB1104700), the National Natural Science Foundation (NSFC, Grant No. 61705227, 61774155, and 11774340), the Jilin Provincial Science & Technology Development Project (20180414019GH), and the Scientific research project of the Chinese Academy of Sciences (QYZDB-SSW-SYS038).

References

1 G. M. Whitesides, *Nature*, 2006, **442**, 368–373.

2 X. Y. Ding, P. Li, S. C. S. Lin, Z. S. Stratton, N. Nama, F. Guo, D. Slotcavage, X. L. Mao, J. J. Shi, F. Costanzo and T. J. Huang, *Lab Chip*, 2013, **13**, 3626–3649.

3 L. R. Shang, Y. Cheng and Y. J. Zhao, *Chem. Rev.*, 2017, **117**, 7964–8040.

4 S. Marre and K. F. Jensen, *Chem. Soc. Rev.*, 2010, **39**, 1183–1202.

5 D. Mark, S. Haeberle, G. Roth, F. von Stetten and R. Zengerle, *Chem. Soc. Rev.*, 2010, **39**, 1153–1182.

6 F. D. Zitzmann, H. G. Jahnke, F. Nitschke, A. G. Beck-Sickinger, B. Abel, D. Belder and A. A. Robitzki, *Lab Chip*, 2017, **17**, 4294–4302.

7 T. O. Mason, T. C. T. Michaels, A. Levin, E. Gazit, C. M. Dobson, A. K. Buell and T. P. J. Knowles, *J. Am. Chem. Soc.*, 2016, **138**, 9589–9596.

8 Y. J. Jan, J. F. Chen, Y. Z. Zhu, Y. T. Lu, S. H. Chen, H. Chung, M. Smalley, Y. W. Huang, J. T. Dong, L. C. Chen, H. H. Yu, J. S. Tomlinson, S. Hou, V. G. Agopian, E. M. Posadas and H. R. Tseng, *Adv. Drug Delivery Rev.*, 2018, **125**, 78–93.

9 M. G. Roper, *Anal. Chem.*, 2016, **88**, 381–394.

10 A. M. Elizarov, *Lab Chip*, 2009, **9**, 1326–1333.

11 W. Xin, T. Wu, T. Zou, Y. Wang, W. Jiang, F. Xing, J. Yang and C. Guo, *Front. Chem.*, 2019, **7**, 395.

12 L. X. Quang, C. Lim, G. H. Seong, J. Choo, K. J. Do and S. K. Yoo, *Lab Chip*, 2008, **8**, 2214–2219.

13 Q. Zhou and T. Kim, *Sens. Actuators, B*, 2016, **227**, 504–514.

14 M. Moskovits, *J. Raman Spectrosc.*, 2005, **36**, 485–496.

15 P. L. Stiles, J. A. Dieringer, N. C. Shah and R. R. Van Duyne, *Annu. Rev. Anal. Chem.*, 2008, **1**, 601–626.

16 K. Kneipp, Y. Wang, H. Kneipp, L. T. Perelman, I. Itzkan, R. Dasari and M. S. Feld, *Phys. Rev. Lett.*, 1997, **78**, 1667–1670.

17 J. Kneipp, H. Kneipp and K. Kneipp, *Chem. Soc. Rev.*, 2008, **37**, 1052–1060.

18 Y. Q. Wang, B. Yan and L. X. Chen, *Chem. Rev.*, 2013, **113**, 1391–1428.

19 R. A. Alvarez-Puebla and L. M. Liz-Marzan, *Small*, 2010, **6**, 604–610.

20 M. Mohamed Shaban, IEEE, Asmaa Gamal Abdel Hady, and Mohamed Serry, Member, IEEE, *IEEE Sens. J.*, 2014, **14**, 436–441.

21 S. Yan, F. Chu, H. Zhang, Y. Yuan, Y. Huang, A. Liu, S. Wang, W. Li, S. Li and W. Wen, *Spectrochim. Acta, Part A*, 2019, **220**, 117113.

22 G. Wang, C. Lim, L. Chen, H. Chon, J. Choo, J. Hong and A. J. deMello, *Anal. Bioanal. Chem.*, 2009, **394**, 1827–1832.

23 E. Chung, R. Gao, J. Ko, N. Choi, D. W. Lim, E. K. Lee, S. I. Chang and J. Choo, *Lab Chip*, 2013, **13**, 260–266.

24 Y. Wang, M. Shang, Y. Wang and Z. Xu, *Anal. Methods*, 2019, **11**, 3966–3973.

25 J. A. Huang, Y. L. Zhang, H. Ding and H. B. Sun, *Adv. Opt. Mater.*, 2015, **3**, 618–633.

26 W. J. Yan, L. K. Yang, J. N. Chen, Y. Q. Wu, P. J. Wang and Z. P. Li, *Adv. Mater.*, 2017, **29**, 1702893.

27 S. Bai, D. Serien, A. M. Hu and K. Sugioka, *Adv. Funct. Mater.*, 2018, **28**, 1706262.

28 M. R. Lee, H. K. Lee, Y. J. Yang, C. S. L. Koh, C. L. Lay, Y. H. Lee, I. Y. Phang and X. Y. Ling, *ACS Appl. Mater. Interfaces*, 2017, **9**, 39584–39593.

29 J. Jeon, N. Choi, H. Chen, J. I. Moon, L. X. Chen and J. Choo, *Lab Chip*, 2019, **19**, 674–681.

30 M. Viehrig, A. H. Thilsted, M. Matteucci, K. Y. Wu, D. Catak, M. S. Schmidt, K. Zor and A. Boisen, *ACS Appl. Mater. Interfaces*, 2018, **10**, 37417–37425.

31 Y. Cheng, J. Xie, K.-H. Lee, R. L. Gaur, A. Song, T. Dai, H. Ren, J. Wu, Z. Sun, N. Banaei, D. Akin and J. Rao, *Sci. Transl. Med.*, 2018, **10**, eaar4470.

32 D. Gosselin, M. N. Belgacem, B. Joyard-Pitiot, J. M. Baumlin, F. Navarro, D. Chaussy and J. Berthier, *Sens. Actuators, B*, 2017, **248**, 395–401.

33 B. B. Xu, Y. L. Zhang, H. Xia, W. F. Dong, H. Ding and H. B. Sun, *Lab Chip*, 2013, **13**, 1677–1690.

34 H. Wang, Y.-L. Zhang, W. Wang, H. Ding and H.-B. Sun, *Laser Photonics Rev.*, 2017, **11**, 1600116.

35 B. Han, Y.-L. Zhang, L. Zhu, X.-H. Chen, Z.-C. Ma, X.-L. Zhang, J.-N. Wang, W. Wang, Y.-Q. Liu, Q.-D. Chen and H.-B. Sun, *Sens. Actuators, B*, 2018, **270**, 500–507.

36 G. L. Roth, C. Esen and R. Hellmann, *Opt. Express*, 2017, **25**, 18442–18450.

37 W. Xiong, Y. S. Zhou, X. N. He, Y. Gao, M. Mahjouri-Samani, L. Jiang, T. Baldacchini and Y. F. Lu, *Light: Sci. Appl.*, 2012, **1**, e6.

38 K. C. Phillips, H. H. Gandhi, E. Mazur and S. K. Sundaram, *Adv. Opt. Photonics*, 2015, **7**, 684–712.

39 K. Sugioka and Y. Cheng, *Light: Sci. Appl.*, 2014, **3**, e149.

40 Y. L. Zhang, Y. Tian, H. Wang, Z. C. Ma, D. D. Han, L. G. Niu, Q. D. Chen and H. B. Sun, *ACS Nano*, 2019, **13**, 4041–4048.

41 C. Florian, E. Skoulas, D. Puerto, A. Mimidis, E. Stratakis, J. Solis and J. Siegel, *ACS Appl. Mater. Interfaces*, 2018, **10**, 36564–36571.

42 K. Yin, S. Yang, X. R. Dong, D. K. Chu, J. A. Duan and J. He, *ACS Appl. Mater. Interfaces*, 2018, **10**, 31433–31440.

43 A. Y. Vorobyev, V. S. Makin and C. L. Guo, *Phys. Rev. Lett.*, 2009, **102**, 234301.

44 E. M. Garcell and C. L. Guo, *Opt. Mater. Express*, 2019, **9**, 1033–1040.

45 A. Y. Vorobyev and C. L. Guo, *Opt. Express*, 2010, **18**, 6455–6460.

46 A. Y. Vorobyev and C. L. Guo, *Appl. Phys. Lett.*, 2009, **94**, 224102.

47 A. Y. Vorobyev and C. L. Guo, *J. Nano Res.*, 2011, **14**, 57–67.

48 B. J. Li, H. Li, L. J. Huang, N. F. Ren and X. Kong, *Appl. Surf. Sci.*, 2016, **389**, 585–593.

49 L. Jiang, A. D. Wang, B. Li, T. H. Cui and Y. F. Lu, *Light: Sci. Appl.*, 2018, **7**, 17134.

50 R. R. Fang, A. Vorobyev and C. L. Guo, *Light: Sci. Appl.*, 2017, **6**, e16256.

51 C. S. R. Nathala, A. Ajami, A. A. Ionin, S. I. Kudryashov, S. V. Makarov, T. Ganz, A. Assion and W. Husinsky, *Opt. Express*, 2015, **23**, 5915–5929.

52 J. Z. Li, S. Ho, M. Haque and P. R. Herman, *Opt. Mater. Express*, 2012, **2**, 1562–1570.

53 W. Cao, L. Jiang, J. Hu, A. D. Wang, X. W. Li and Y. F. Lu, *ACS Appl. Mater. Interfaces*, 2018, **10**, 1297–1305.

54 K. Yin, D. K. Chu, X. R. Dong, C. Wang, J. A. Duan and J. He, *Nanoscale*, 2017, **9**, 14229–14235.

55 R. N. Wenzel, *Ind. Eng. Chem.*, 1936, **28**, 988–994.

56 J. A. M. R. R. Rye, Jr. and F. G. Yost, *Langmuir*, 1996, **12**, 555–565.

57 J. Bonse, S. Hohm, S. V. Kirner, A. Rosenfeld and J. Kruger, *IEEE J. Sel. Top. Quantum Electron.*, 2017, **23**, 9000615.

58 P. Zuo, L. Jiang, X. Li, B. Li, P. Ran, X. J. Li, L. T. Qu and Y. F. Lu, *ACS Sustainable Chem. Eng.*, 2018, **6**, 7704–7714.

59 X. F. Ding, L. T. Kong, J. Wang, F. Fang, D. D. Li and J. H. Liu, *ACS Appl. Mater. Interfaces*, 2013, **5**, 7072–7078.